




Host galaxies of merging compact objects: mass, star formation rate, metallicity, and colours

M. Celeste Artale ¹★, Michela Mapelli,^{1,2,3,4} Nicola Giacobbo ^{2,3,4},
Nadeen B. Sabha,¹ Mario Spera ^{1,2,3,4,5,6}, Filippo Santoliquido²
and Alessandro Bressan⁷

¹*Institut für Astro- und Teilchenphysik, Universität Innsbruck, Technikerstrasse 25/8, A-6020 Innsbruck, Austria*

²*Physics and Astronomy Department Galileo Galilei, University of Padova, Vicolo dell'Osservatorio 3, I-35122 Padova, Italy*

³*INAF-Osservatorio Astronomico di Padova, Vicolo dell'Osservatorio 5, I-35122 Padova, Italy*

⁴*INFN-Padova, Via Marzolo 8, I-35131 Padova, Italy*

⁵*Center for Interdisciplinary Exploration and Research in Astrophysics (CIERA), Evanston, IL 60208, USA*

⁶*Department of Physics & Astronomy, Northwestern University, Evanston, IL 60208, USA*

⁷*Scuola Internazionale Superiore di Studi Avanzati (SISSA), Via Bonomea 265, I-34136 Trieste, Italy*

Accepted 2019 May 15. Received 2019 April 19; in original form 2019 February 21

ABSTRACT

Characterizing the properties of the host galaxies of merging compact objects provides essential clues to interpret current and future gravitational-wave detections. Here, we investigate the stellar mass, star formation rate (SFR), metallicity, and colours of the host galaxies of merging compact objects in the local Universe by combining the results of MOBSE population-synthesis models together with galaxy catalogues from the EAGLE simulation. We predict that the stellar mass of the host galaxy is an excellent tracer of the merger rate per galaxy n_{GW} of double neutron stars (DNSs), double black holes (DBHs), and black hole–neutron star binaries (BHNSs). We find a significant correlation also between n_{GW} and SFR. As a consequence, n_{GW} correlates also with the r -band luminosity and with the $g - r$ colour of the host galaxies. Interestingly, $\gtrsim 60$ per cent, $\gtrsim 64$ per cent, and $\gtrsim 73$ per cent of all the DNSs, BHNSs, and DBHs merging in the local Universe lie in early-type galaxies, such as NGC 4993. We predict a local DNS merger rate density of $\sim 238 \text{ Gpc}^{-3} \text{ yr}^{-1}$ and a DNS merger rate $\sim 16\text{--}121 \text{ Myr}^{-1}$ for Milky Way-like galaxies. Thus, our results are consistent with both the DNS merger rate inferred from GW170817 and the one inferred from Galactic DNSs.

Key words: black hole physics – gravitational waves – methods: numerical – stars: mass-loss.

1 INTRODUCTION

The direct detection of gravitational waves (GWs) from LIGO (Aasi et al. 2015) and Virgo (Acernese et al. 2015) has opened a new perspective to investigate the nature of merging compact objects. Eleven GW sources have been detected so far. Ten of them are identified as double black holes (DBHs; Abbott et al. 2016a,b,c,d, 2017a; The LIGO Scientific Collaboration & the Virgo Collaboration 2018a; The LIGO Scientific Collaboration & The Virgo Collaboration 2018b), and one as a double neutron star (DNS; Abbott et al. 2017b,c). The number of detections is expected to increase significantly in the near future, with the third observing run, and black hole–neutron star systems (BHNS) might also be detected (Giacobbo & Mapelli 2018; Mapelli & Giacobbo 2018).

Several mechanisms have been proposed to explain the formation of merging black holes (BHs) and neutron stars (NSs). The evolution

of massive stellar binaries in the field can lead to the formation of merging compact objects, especially if driven by a common envelope phase (Tutukov & Yungelson 1973; Flannery & van den Heuvel 1975; Bethe & Brown 1998; Portegies Zwart & Yungelson 1998; Portegies Zwart & McMillan 2000; Belczynski, Kalogera & Bulik 2002; Perna & Belczynski 2002; Voss & Tauris 2003; Podsiadlowski et al. 2004, 2005; Belczynski et al. 2006, 2007, 2008; Bogomazov, Lipunov & Tutukov 2007; Moody & Sigurdsson 2009; Dominik et al. 2012, 2013, 2015; Mapelli et al. 2013; Mennekens & Vanbeveren 2014; Tauris, Langer & Podsiadlowski 2015; Belczynski et al. 2016; Eldridge & Stanway 2016; Mapelli et al. 2017; Stevenson et al. 2017; Tauris et al. 2017; Chruslinska et al. 2018; Giacobbo & Mapelli 2018, 2019; Giacobbo, Mapelli & Spera 2018; Kruckow et al. 2018; Mapelli & Giacobbo 2018; Mapelli et al. 2018; Shao & Li 2018; Spera et al. 2019) or by chemically homogeneous evolution (de Mink & Belczynski 2015; de Mink & Mandel 2016; Marchant et al. 2016). Alternative evolutionary channels are dynamical formation in star clusters (Kulkarni, Hut & McMillan 1993; Sigurdsson & Hernquist 1993; Sigurdsson &

* E-mail: Maria.Artale@uibk.ac.at

Phinney 1995; Portegies Zwart & McMillan 2000; Colpi, Mapelli & Possenti 2003; O’Leary et al. 2006; Sadowski et al. 2008; O’Leary, Kocsis & Loeb 2009; Banerjee, Baumgardt & Kroupa 2010; Downing et al. 2010, 2011; Mapelli et al. 2013; Mapelli & Zampieri 2014; Ziosi et al. 2014; Rodriguez et al. 2015; Antonini & Rasio 2016; Hurley et al. 2016; Kimpson et al. 2016; Mapelli 2016; O’Leary, Meiron & Kocsis 2016; Rodriguez, Chatterjee & Rasio 2016; Askar et al. 2017; Banerjee 2017; Zevin et al. 2017; Askar, Arca Sedda & Giersz 2018; Banerjee 2018; Kumamoto, Fujii & Tanikawa 2019; Rastello et al. 2019; Rodriguez et al. 2018; Samsing 2018; Antonini, Gieles & Gualandris 2019; Di Carlo et al. 2019) or in galactic nuclei (O’Leary et al. 2009; McKernan et al. 2012; Bartos et al. 2017; Kelley, Blecha & Hernquist 2017; Stone, Metzger & Haiman 2017; Rasskazov & Kocsis 2019).

The sky localization of GW sources and the characterization of their host galaxies are crucial to identify the most likely formation mechanism. Given current uncertainty on sky localization inferred from GW data (still of the order of tens of square degrees in the best case; see e.g. Abbott et al. 2018), the detection of an electromagnetic counterpart associated with the GW event is essential to localize the host galaxy.

The spectacular detection of the counterpart of GW170817, sweeping almost the entire electromagnetic spectrum from radio to gamma-ray wavelengths (Abbott et al. 2017d; Abbott et al. 2017e; Alexander et al. 2017; Chornock et al. 2017; Coulter et al. 2017; Cowperthwaite et al. 2017; Goldstein et al. 2017; Margutti et al. 2017; Nicholl et al. 2017; Pian et al. 2017; Soares-Santos et al. 2017; Savchenko et al. 2017) has led to the unique identification of the host galaxy, NGC4993. This is an early-type galaxy at redshift $z \sim 0.009783$ (Levan et al. 2017), which probably underwent a major merger recently, with stellar mass of $0.3\text{--}1.2 \times 10^{11} M_{\odot}$ and metallicity in the range of 20–100 per cent the solar metallicity (Im et al. 2017).

In contrast, none of the GW events interpreted as DBH mergers was associated with an electromagnetic detection and thus their host galaxies were not identified. Hence, theoretical models are required to investigate the environment of merging DBHs and BHNSs.

A way to explore the nature of host galaxies of merging compact objects is by combining galaxy formation models with binary population synthesis. With this approach, we can reconstruct the properties of simulated host galaxies (e.g. mass, star formation rate, galaxy type) and possibly we can inform the low-latency search for electromagnetic counterparts (Del Pozzo et al. 2018) or, even if the electromagnetic counterpart is not observed, we can infer astrophysically motivated criteria to localize the most likely host galaxy of a GW event (Mapelli et al. 2018).

The main challenge of this approach is the extreme physical range between galaxy formation and compact object binary formation. Several works have attempted to address this issue by (semi)analytical models or by cosmological simulations (e.g. O’Shaughnessy, Kalogera & Belczynski 2010; Belczynski et al. 2016; Dvorkin et al. 2016; Lamberts et al. 2016; O’Shaughnessy et al. 2017; Schneider et al. 2017; Cao, Lu & Zhao 2018; Elbert, Bullock & Kaplinghat 2018; Lamberts et al. 2018; Mapelli et al. 2018; Perna et al. 2018; Eldridge, Stanway & Tang 2019; Mapelli et al. 2019; Marassi et al. 2019; Safarzadeh & Berger 2019).

Using a sample of zoom-in simulations, O’Shaughnessy et al. (2017) discuss the impact of the assembly history of galaxies on DBH mergers and suggest that DBHs are more likely to form in nearby metal-poor dwarf galaxies. Cao et al. (2018) make an exhaustive analysis of the host galaxies of DBHs by using the cosmological N -body simulation Millennium-II with semi-analytical

galaxy formation recipes from Guo et al. (2011). Assuming different delay times for DBHs, they find that at $z = 0.3$ massive merging DBHs (with total mass $\gtrsim 50 M_{\odot}$) formed at high redshift reside in galaxies with stellar mass $\sim 4.7 \times 10^{10} M_{\odot}$, while DBHs formed recently are located in $\sim 10^7\text{--}10^9 M_{\odot}$ galaxies.

Lamberts et al. (2018) investigate DBH systems in Milky Way-type galaxies, combining zoom-in simulations with population synthesis models. Interestingly, they find that one-third of the DBHs were formed ex-situ of the main galaxy, in satellite galaxies that eventually merged.

Combining the results of population synthesis simulations with the cosmological box Illustris-1 (Vogelsberger et al. 2014), Mapelli et al. (2018) explore the host galaxies of merging DNSs, DBHs, and BHNSs in the local Universe. They find that DNSs tend to form and merge in galaxies with stellar mass $10^9\text{--}10^{12} M_{\odot}$ with short delay times. In contrast, BHNSs and DBHs form preferentially in low-mass galaxies ($< 10^{10} M_{\odot}$), but merge either in massive or low-mass galaxies with longer delay times than DNS sources. These results originate from the different metallicity dependence of merging compact objects: DBHs and BHNSs are expected to form more efficiently from metal-poor progenitors, while DNSs form almost independently of progenitor’s metallicity (Giacobbo & Mapelli 2018).

In this work, we investigate the properties of the host galaxies of merging DBHs, DNSs, and BHNS in the local Universe. We combine the galaxy catalogues from the hydrodynamical cosmological simulation EAGLE (Schaye et al. 2015) with the catalogues of merging compact objects from the population synthesis code MOBSE (Giacobbo et al. 2018).

Our methodology is similar to the one presented by Mapelli et al. (2017, 2018), but we adopt a cosmological box with a resolution ~ 5.5 higher. This enables us to probe host galaxies to lower stellar mass (down to $\sim 10^7 M_{\odot}$), which are unresolved in the Illustris-1 simulation adopted by Mapelli et al. (2017). Moreover, the sub-grid physical models adopted in the EAGLE and in the Illustris simulations are drastically different. Thus, we also want to understand the uncertainties introduced in our work by the choice of a cosmological simulation.

This paper is organized as follows. In Section 2 we describe the main properties of EAGLE and MOBSE, while the methodology is explained in Section 2.3. We investigate the connection between the GW sources and the star formation rate, stellar mass, and metallicity of the host galaxies in Section 3. In Section 4, we discuss the implications of our results on the merger rate in late-type and early-type galaxies. Our main conclusions are discussed in Section 5.

2 METHODS

We compute the number of DNSs, DBHs, and BHNSs by combining the results from the population synthesis code MOBSE (Giacobbo et al. 2018) with galaxy catalogues from the hydrodynamical cosmological simulation EAGLE. In this section, we present the general features of these codes.

2.1 Population synthesis code: MOBSE

The population synthesis code MOBSE (Giacobbo et al. 2018) represents an upgrade of the BSE code (Hurley, Pols & Tout 2000; Hurley, Tout & Pols 2002) including new prescriptions for stellar winds (see Vink, de Koter & Lamers 2001; Vink & de Koter 2005; Chen et al. 2015), core-collapse supernovae (SNe) based on Fryer

et al. (2012), and pair-instability and pulsational pair-instability SNe (Spera & Mapelli 2017; Woosley 2017)

In particular, MOBSE describes the mass-loss by stellar winds of massive hot stars (O- and B-type main sequence stars, Wolf-Rayet stars, and luminous blue variable stars) as $\dot{M} \propto Z^\beta$, where β is defined in the following way:

$$\beta = \begin{cases} 0.85 & \text{if } \Gamma_e < 2/3 \\ 2.45 - 2.40 \Gamma_e & \text{if } 2/3 \leq \Gamma_e \leq 1 \\ 0.05 & \text{if } \Gamma_e > 1. \end{cases} \quad (1)$$

Here Γ_e is the electron-scattering Eddington ratio, expressed as (see equation 8 of Gräfener et al. 2011):

$$\log \Gamma_e = -4.813 + \log(1 + X_H) + \log(L/L_\odot) - \log(M/M_\odot). \quad (2)$$

In equation (2), X_H is the Hydrogen fraction, L is the star luminosity, and M is the star mass.

Accounting for the dependence of mass-loss on both metallicity (Z ; Vink et al. 2001) and Eddington ratio (Vink 2017) is a key ingredient to predict the final mass of a compact object (Mapelli, Colpi & Zampieri 2009; Belczynski et al. 2010; Mapelli et al. 2010; Mapelli et al. 2013; Spera, Mapelli & Bressan 2015). In fact, massive metal-poor stars are predicted to lose much less mass by stellar winds than metal-rich stars, ending their life with larger cores and larger envelopes. This implies that massive metal-poor stars are more likely to directly collapse into BHs, without an SN explosion, giving birth to more massive remnants than metal-rich stars.

In MOBSE, the final mass of the compact object depends on the Carbon–Oxygen core mass and on the final mass of the progenitor star as described in Fryer et al. (2012). In particular, in this paper we make use of the rapid core–collapse SN model described by Fryer et al. (2012). MOBSE also includes a description of electron-capture SNe, as detailed in Giacobbo & Mapelli (2019). Massive stars developing a Helium core between 32 and 64 M_\odot are expected to develop pulsational pair instability, which is modelled as described in Spera & Mapelli (2017). Finally, stars with Helium core in the 64–135 M_\odot range are expected to undergo pair instability and to be completely disrupted, leaving no compact object.

These prescriptions produce a mass spectrum of compact objects as shown in Fig. 1. The mass distribution shows a dearth of compact objects with mass between ~ 2 and $\sim 5 M_\odot$, consistent with the mass gap between NSs and BHs suggested by Özel et al. (2010) and Farr et al. (2011). The maximum mass of BHs in this model is $\sim 65 M_\odot$ (at metallicity $Z = 0.0002$), although Giacobbo et al. (2018) and Giacobbo & Mapelli (2018) show that only BHs with mass $\lesssim 40 M_\odot$ are able to merge by GW emission within a Hubble time.

In this work, we use the catalogue of merging compact objects corresponding to the run named as CC15 α 5 from Giacobbo & Mapelli (2018), also implemented in Mapelli et al. (2018). This run matches the cosmic merger rate reported by recent LIGO–Virgo results (see fig. 15 in Giacobbo & Mapelli 2018; Giacobbo & Mapelli 2018). It also matches the expected merger rate of DNSs in the Milky Way, according to the estimate by Pol, McLaughlin & Lorimer (2019). In this run we adopt high efficiency of common-envelope ejection ($\alpha = 5$) and low SN kicks using a Maxwellian curve with root mean square $\sigma = 15 \text{ km s}^{-1}$. Low natal kicks are consistent also with the orbital properties of some DNSs in the Milky Way (van den Heuvel 2007; Beniamini & Piran 2016), with the presence of r-process material in ultrafaint dwarf galaxies (Beniamini, Hotokezaka & Piran 2016) and with several families of

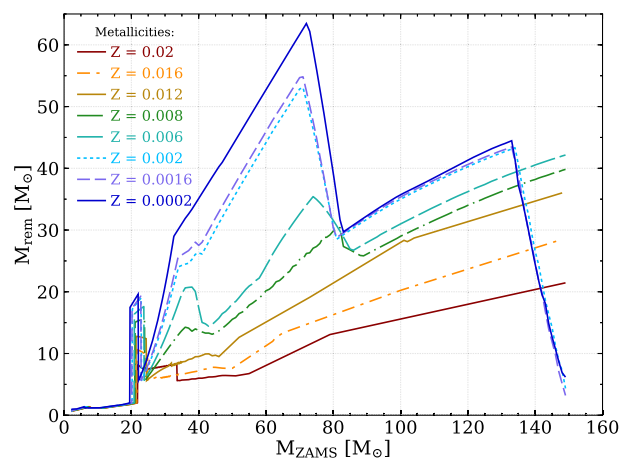


Figure 1. Mass of the compact object (M_{rem}) as a function of the mass of the progenitor star (M_{ZAMS}) for eight metallicities between $Z = 0.02$ and 0.0002 . See Giacobbo et al. (2018) for details on this model.

X-ray binaries (e.g. Pfahl et al. 2002; Knigge, Coe & Podsiadlowski 2011; Tauris et al. 2017, and references therein).

The simulation is composed of 12 sub-sets at different metallicities $Z = 0.0002, 0.0004, 0.0008, 0.0012, 0.0016, 0.002, 0.004, 0.006, 0.008, 0.012, 0.016$ and 0.02 . We adopt as solar metallicity $Z_\odot = 0.02$. For each sub-set we simulate 10^7 stellar binaries, hence the total number of binaries is 1.2×10^8 .

We combine the catalogue of merging compact objects obtained with MOBSE with the galaxy catalogue from the cosmological hydrodynamical simulation EAGLE. We describe the main properties of EAGLE in the following section.

2.2 The EAGLE simulation

The EAGLE simulation suite (Crain et al. 2015; Schaye et al. 2015) is a set of cosmological hydrodynamical simulations that were run with a modified version of GADGET-3 code. In this work we use the simulation labelled as RecalL0025N0752 available on the SQL data base (see McAlpine et al. 2016).¹ This run represents the highest resolution available of EAGLE suite, and at the same time, contains a statistical sample of galaxies with different morphologies, stellar masses, and star formation rates.

The RecalL0025N0752 run represents a periodic box of 25 Mpc side that initially contains 752^3 gas and dark matter particles with masses of $m_{\text{gas}} = 2.26 \times 10^5 M_\odot$ and $m_{\text{DM}} = 1.21 \times 10^6 M_\odot$. Henceforth, we refer to this run simply as EAGLE. The simulation was run from $z = 127$ up to $z \sim 0$, adopting the Λ CDM cosmology with parameters inferred from Planck Collaboration XVI (2014) ($\Omega_m = 0.2588$, $\Omega_\Lambda = 0.693$, $\Omega_b = 0.0482$, and $H_0 = 100 h \text{ km s}^{-1} \text{ Mpc}^{-1}$ with $h = 0.6777$). We have selected the RecalL0025N0752 EAGLE simulation since it enables us to investigate host galaxies with a lower stellar mass (10^7 – $10^8 M_\odot$) not well resolved in the larger (100 Mpc) EAGLE box.

The EAGLE simulation includes different sub-grid models to account for different processes behind galaxy formation such as star formation, radiative cooling and heating, stellar evolution, chemical enrichment, UV/X-ray ionizing background, AGB stars and SN feedback, and AGN feedback. For this run, the parameters of the sub-grid models are calibrated to reproduce the galaxy sizes at $z \sim$

¹<http://icc.dur.ac.uk/Eagle/>, <http://virgo.dur.ac.uk/data.php>

0, the observed stellar mass function, and the relation between the black hole and stellar masses (see Schaye et al. 2015, for further details).

From the data base, we can obtain the information of the stellar particles and the galaxy properties such as the total stellar mass, the metallicity of the star-forming gas, and the star formation rate. In this work we select all galaxies above $M_* > 10^7 M_\odot$ which corresponds to have at least ~ 44 stellar particles within the galaxy.

We also explore the colours of the host galaxies of DNSs by computing their colour–magnitude diagram. For this we use the dust attenuated absolute g and r bands in AB magnitudes in the rest frame of galaxies. These magnitudes were computed using the radiative transfer code SKIRT for galaxies with stellar mass $M_* > 10^{8.5} M_\odot$, which contains more than 250 dust particles. The details of the procedure are described in Camps et al. (2016, 2018), and the magnitudes are provided in the EAGLE data base.

2.3 Monte Carlo Method

To compute the number of merging compact objects within the host galaxies in the nearby Universe, we first combine the results from the population synthesis run CC15 α 5 with the information of the stellar particles from EAGLE. For this, we follow the methodology presented in Mapelli et al. (2017) (see Section 2.3 of the aforementioned work), also implemented in Mapelli & Giacobbo (2018) and Mapelli et al. (2018). In this section we summarize the main concepts of this method.

From the EAGLE simulation, we first select the stellar particles formed in each snapshot as the progenitors of merging compact objects. We use the initial mass m_* , formation time t_* , and metallicity Z_* of each stellar particle, and we find the metallicity that best matches Z_* among the 12 simulated metallicities of run CC15 α 5.

For each sub-set of CC15 α 5, we use the total initial stellar mass M_{MOBSE} , and the total number of merging compact objects N_{MOBSE} (corresponding to DBHs, DNSs, or BHNS). Then for each stellar particle, we combine this information and compute the number of merging compact objects (n_{mco}) as

$$n_{\text{mco}} = N_{\text{MOBSE}} \frac{m_*}{M_{\text{MOBSE}}} f_{\text{corr}} f_{\text{bin}}, \quad (3)$$

where the parameter $f_{\text{corr}} = 0.285$ is a correction factor accounting that the primary stars are $m_p \geq 5 M_\odot$, while $f_{\text{bin}} = 0.5$ is the binary fraction (we assume 50 per cent of stars are in binaries).

Then, we randomly select n_{mco} merging compact objects from the simulated stellar population sub-set with mass M_{MOBSE} and we associate them with the corresponding EAGLE stellar particle. Due to the resolution of the EAGLE suite selected in this work, most stellar particles have $n_{\text{mco}} < 1$ (i.e. they produce less than one merging compact object). Thus, we impose that if $n_{\text{mco}} < 1$ for a given particle, the next stellar particle we consider inherits the value of n_{mco} from the previous particle in addition to its own value of n_{mco} , till n_{mco} becomes ≥ 1 . We assign the merging compact object to the first stellar particle for which $n_{\text{mco}} \geq 1$ and then we reset the value of n_{mco} . For each merging compact object selected we save its properties such as the masses of the two compact objects and the delay time.

For each merging compact object selected as above, we estimate the lookback time of the merger, by combining the formation time of the stellar particle (t_{form}) with the time between the formation of the progenitor binary system and the merger of the two compact objects (delay time, t_{delay}), as $t_{\text{merg}} = t_{\text{form}} - t_{\text{delay}}$. This procedure allows us to follow the position of the stellar particles from EAGLE

simulation across cosmic time. Hence, it is possible to identify the properties of host galaxies where merging compact objects form and merge.

Since we want to investigate merging compact objects in the local Universe, we only select the merging compact objects corresponding to $z \lesssim 0.1$ (i.e. the snapshots corresponding to $z = 0$ and $z = 0.1$). Hence, in this work we investigate the properties of the host galaxies at the time compact binary systems merge.

We note that double compact objects can be formed at early stages of the Universe with long delay times, and merge at $z \lesssim 0.1$ (Cao et al. 2018; Mapelli et al. 2018). In the following analysis, we will consider only those galaxies that contain at least one binary compact object merging at $z \lesssim 0.1$ (i.e. galaxies that do not host merging compact objects are not shown).

3 RESULTS

3.1 Mass–metallicity relation

Fig. 2 shows the mass–metallicity relation for the host galaxies of DNSs, DBHs, and BHNSs. As expected, massive galaxies in the EAGLE simulation are metal-rich compared with low-mass galaxies, reproducing the observed trend (Schaye et al. 2015; De Rossi et al. 2017). The black lines mark the mass–metallicity range of NGC 4993, the host galaxy of GW170817 reported by Im et al. (2017). Although the uncertainty on the metallicity of NGC 4993 is extremely large, this galaxy seems to be remarkably metal poor with respect to the average value of the galaxies in our sample. The mass of NGC 4993 matches the mass of the most massive galaxies in our sample.

The merger rate per galaxy (n_{GW} , i.e. the number of compact object mergers per galaxy per unit time) of DNSs, BHNSs, and DBHs strongly correlates with the stellar mass of the host galaxy at the time of merger. Interestingly, even considering the large scatter in metallicity at a given stellar mass, the stellar mass content of galaxies shows to be a fundamental tracer of the merger rate.

3.2 Host galaxy stellar mass

The left-hand panel of Fig. 3 shows the merger rate per galaxy (n_{GW}) as a function of the stellar mass of the host galaxy. We find a very strong correlation between host galaxy mass and merger rate. This relation is steeper for DNSs than for DBHs and BHNSs, indicating that the dependence on stellar mass is more prominent for DNSs. To quantify this difference, we fit the relation $\log(n_{\text{GW}}) = a_{M_*} \log(M_*) + b_{M_*}$ with a least-squares linear regression.²

Table 1 shows the fit results. The correlation of the DNS merger rate per galaxy with the mass of the host galaxy is steeper than linear for DNSs, while it is sensibly shallower than linear for BHNSs and DBHs.

We find that galaxies with stellar mass $M_* = 10^{11} M_\odot$ host ~ 4.4 and ~ 5.2 more DNS mergers per Gyr than DBH and BHNS mergers, respectively. For galaxies with mass $M_* = 10^9 M_\odot$ the difference is lower, reaching a factor of ~ 1.9 . Our results indicate that massive galaxies are the best place to look for merging DNSs. This result

²We use the module polyfit from numpy, which minimizes the squared error $E = \sum_{j=0}^k |p(x, k) - y_j|^2$ where $p(x, k)$ represents the linear function adopted, and y_j refers to the data points (see Olyphant 2006; van der Walt, Colbert & Varoquaux 2011). The reported errors are standard deviations computed using the diagonal of the covariance matrix for each parameter.

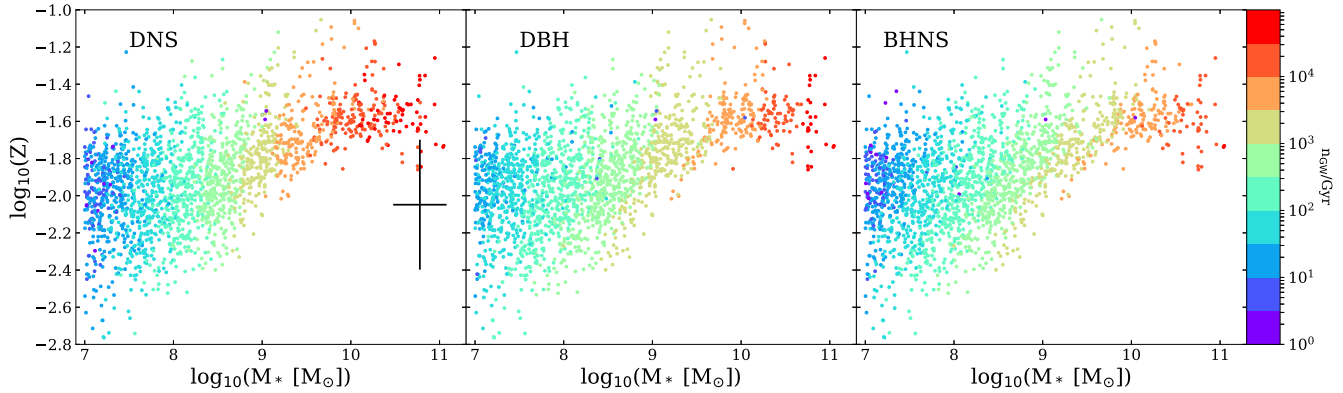


Figure 2. Mass–metallicity relation of the host galaxies of merging DNSs (left-hand panel), DBHs (middle panel), and BHNSs (right-hand panel). Each point represents an individual galaxy from the EAGLE catalogue. The colour code represents the local merger rate per galaxy n_{GW} (i.e. the total number of merging compact objects per each galaxy per redshift bin, from $z = 0$ to $z = 0.1$). On the left-hand panel, the black lines represent the range of masses and metallicities computed for the galaxy NGC 4993, the host galaxy of GW170817 (see, Im et al. 2017).

is in agreement with Mapelli et al. (2018), which finds that the host galaxies of merging DNSs have preferentially stellar mass $> 10^9 M_{\odot}$.

For a fixed stellar mass, metal-poor galaxies have a higher DBH and BHNS merger rate per galaxy than metal-rich ones. This is apparent from the right-hand panel of Fig. 3, also shown in Fig. 2. This dependence seems to be less significant for the host galaxies of DNSs. From the right-hand panel of Fig. 3 we find that low-mass galaxies have a more efficient merger rate per galaxy of DBHs and BHNS systems, while for DNSs this trend is less significant.

3.3 Star formation rate

Fig. 4 shows the merger rate per galaxy (n_{GW}) as a function of the SFR of the host galaxy. We find that the merger rate per galaxy correlates also with the SFR.

We fit the relation between the merger rate per galaxy and the SFR of the host galaxy using the same methodology previously described. Hence, we adopt the relation $\log(n_{\text{GW}}) = a_{\text{SFR}} \log(\text{SFR}) + b_{\text{SFR}}$ (see Table 1). Also in this case, the correlation is steeper for DNSs than for DBHs and BHNSs. Moreover, the correlation between merger rate per galaxy and SFR is significantly less steep than the correlation between merger rate per galaxy and stellar mass. The former correlation has also a larger scatter than the latter one.

It is interesting to note that for a fixed SFR, metal-rich galaxies are associated with a higher merger rate per galaxy than metal-poor ones (see Fig. 4). However, this result must not be misunderstood, since selecting galaxies with a fixed SFR means putting together a wide range of stellar masses. As stated by Mannucci et al. (2010), galaxies in the local Universe show a fundamental relation between the stellar mass, the gas-phase metallicity, and the SFR. At a fixed stellar mass, galaxies with high SFR have a lower metallicity than low SFR galaxies. Moreover, at fixed SFR, massive galaxies are more metal rich compared with low-mass galaxies. To clarify this and to make more explicit the connection with the fundamental metallicity relation, Fig. 5 shows the relation between SFR, stellar mass, and merger rate per galaxy for the host galaxies of DNSs. Overall, galaxies with a higher SFR tend to be more massive than galaxies with a low SFR, as shown by Mannucci et al. (2010). Hence, the correlation between merger rate per galaxy and SFR is likely a consequence of the correlation between SFR and stellar mass of the host galaxy. Therefore, our results reflect the strong

correlation between the merger rate per galaxy and the stellar mass of the host galaxy.

3.4 Host galaxy metallicity

In Fig. 6, we show the merger rate per galaxy as a function of the metallicity for the host galaxies of merging DNSs, DBHs, and BHNSs. We also include the linear regression fits computed as $\log(n_{\text{GW}}) = a_Z \log(Z) + b_Z$ (see the parameters obtained in Table 1). Metal-rich galaxies have a higher merger rate since they also represent the most massive ones. This result holds not only for DNSs (which are almost not affected by progenitor’s metallicity), but also for DBHs and BHNSs, which form predominantly from metal-poor progenitors. This indicates that the metallicity of the galaxy where these binaries merge is very different from the metallicity of the galaxy where these binaries formed. Overall, there is a very large scatter in the correlation between Z and n_{GW} .

3.5 The colour–magnitude diagram of the host galaxies of DNSs

It is well known that the colour is a good tracer of SFR in galaxies, while luminosity correlates with their stellar mass. Hence, exploring the colour–magnitude of the host galaxies can provide us information about where it is more likely to detect a GW event. In this section we focus only on the host galaxies where DNSs merge, since only the host galaxy of GW170817 has been identified.

Fig. 7 shows the colour–magnitude diagram of the host galaxies of DNSs at their merger time, derived from the EAGLE galaxy catalogue. The sample of galaxies in this figure is smaller than the sample considered in previous figures, because colours are only provided for galaxies with stellar masses above $10^{8.5} M_{\odot}$, containing more than 250 dust particles (see Section 2.3).

We find that brighter (massive) galaxies host a higher number of merging DNSs per Gyr, irrespective of their colour. Our results confirm that the stellar mass is a much more important tracer of the merger rate than the SFR. We also include the colour–magnitude of NGC 4993, the host galaxy of GW170817 computed by Blanchard et al. (2017). The reported magnitudes were converted to absolute and K -corrected to make a proper comparison with EAGLE galaxies.

From Fig. 7 it is apparent that NGC 4993 falls in the region of the colour–magnitude diagram associated with the higher merger

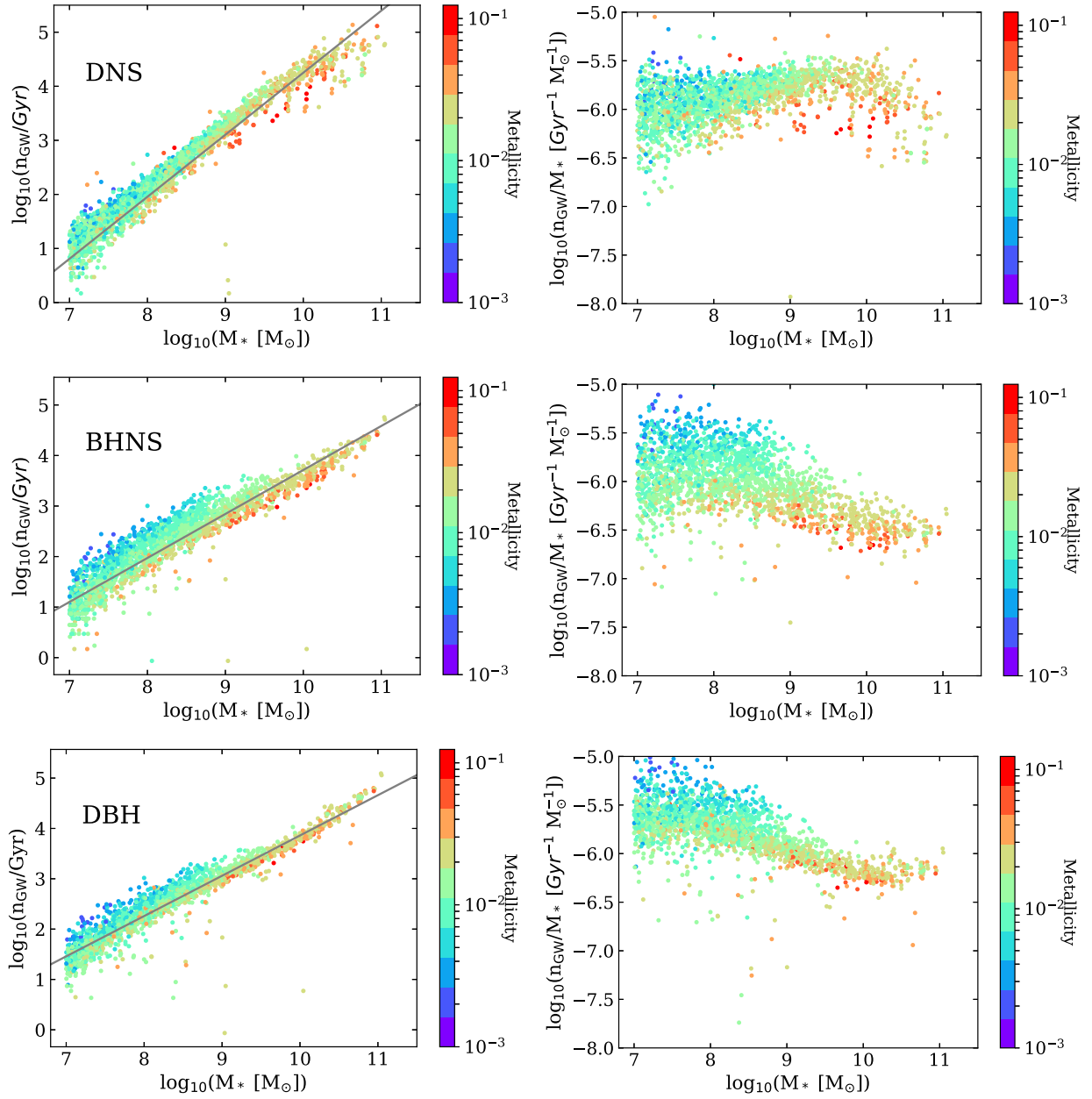


Figure 3. Left-hand panel: Merger rate per galaxy as a function of the stellar mass of the host galaxy. Top panel: DNSs; middle panel: BHNSs; bottom panel: DBHs. We include the fits of $\log(n_{\text{GW}}/\text{Gyr}) = a_{M_*} \log(M_*) + b_{M_*}$. Right-hand panel: Merger rate per galaxy normalized to the galaxy mass as a function of the stellar mass of the host galaxy. In all the plots each point represents an individual galaxy from the EAGLE catalogue. The colour code indicates the metallicity of the host galaxy.

Table 1. Results of the linear fit of the compact-object (CO) merger rate per galaxy (n_{GW}) as a function of the stellar mass (M_*), the SFR, and the metallicity.

Merging COs	a_{M_*}	b_{M_*}	a_{SFR}	b_{SFR}	a_Z	b_Z
DNSs	1.15 ± 0.08	-7.22 ± 0.22	0.90 ± 0.10	4.02 ± 0.14	2.01 ± 0.27	6.23 ± 0.37
DBHs	0.80 ± 0.07	-4.14 ± 0.19	0.65 ± 0.09	3.69 ± 0.13	1.29 ± 0.24	4.99 ± 0.33
BHNSs	0.87 ± 0.08	-4.99 ± 0.22	0.70 ± 0.09	3.56 ± 0.13	1.09 ± 0.26	4.38 ± 0.35

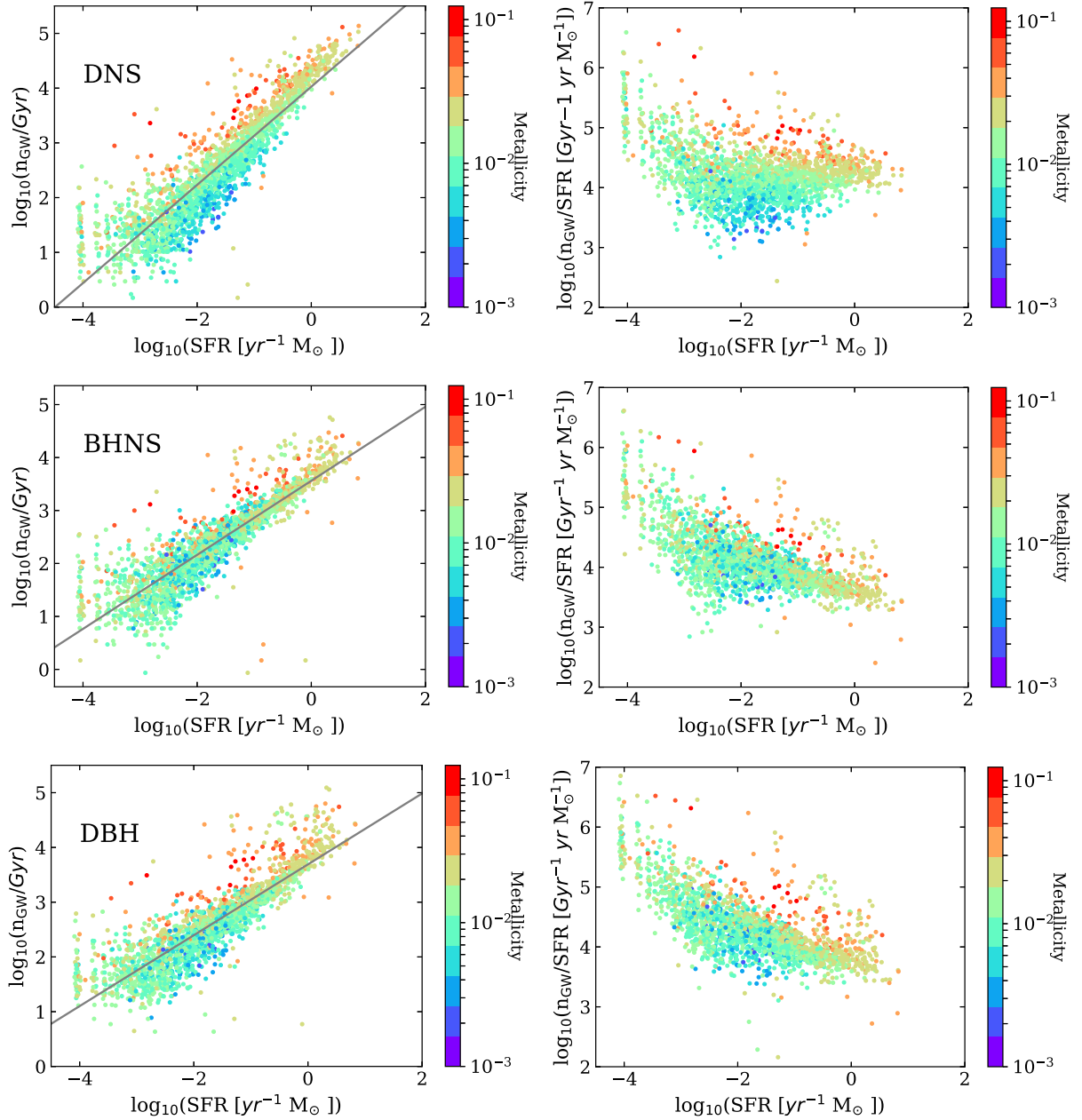


Figure 4. Left-handpanel: Merger rate per galaxy as a function of the star formation rate (SFR) for DNSs, BHNSs, and DBHs. We include the fits of $\log(n_{\text{GW}}/\text{Gyr}) = a_{\text{SFR}} \log(\text{SFR}) + b_{\text{SFR}}$. Right-hand panel: Merger rate per galaxy normalized to the SFR, as a function of the SFR of the host galaxy. Each point represents an individual galaxy from the EAGLE catalogue. The colour code represents the metallicity of the host galaxy.

rate per galaxy in the local Universe. This suggests that NGC 4993 is also one of the galaxies where it is more likely to detect DNS mergers, although to quantitatively support this statement we need to include observational selection effects and to convolve them with the instrumental range of GW detectors (Artale et al., in preparation).

4 DISCUSSION

We find a very strong correlation between the merger rate per galaxy n_{GW} and the stellar mass of the host galaxy M_* where the two compact objects merge. We find also a significant correlation

between n_{GW} and the SFR, and a very mild correlation between n_{GW} and the host galaxy metallicity.

It is worth noticing that the host galaxy where the two compact objects merge is not necessarily the same as the host galaxy where their progenitor binary star formed, because the initial host galaxy might have merged into a larger galaxy before the two compact objects reached coalescence (Mapelli et al. 2018). Moreover, even if the galaxy where the compact object merger occurs is the same as the galaxy where the progenitor binary formed, its SFR, stellar mass, and metallicity at the time of the merger might be significantly different from the SFR, stellar mass, and metallicity at the time of the formation of the stellar progenitors.

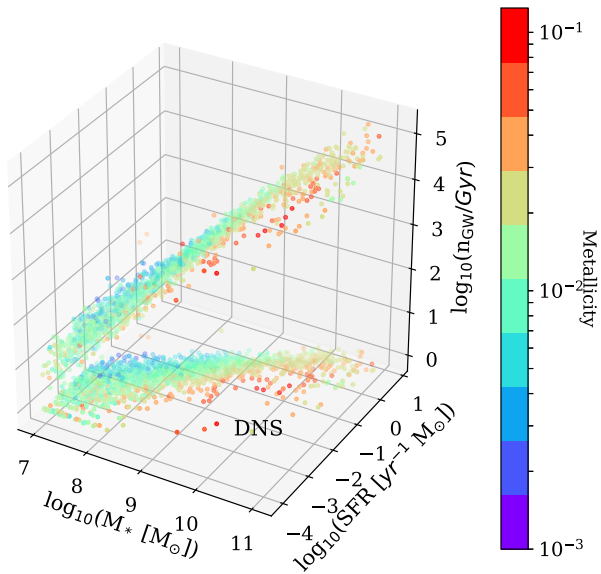


Figure 5. 3-D map of the merger rate per galaxy (z -axis) as a function of SFR (x -axis) and stellar mass (y -axis) for the host galaxies of DNSs. Each point represents an individual galaxy from the EAGLE catalogue. The colour-code represents the metallicity of the galaxy. The points are also projected in the SFR – M_* relation.

Thus, even if our model enforces a strong correlation between the merger rate of compact objects and the SFR at the time of the progenitor binary formation, this does not imply that there is still a correlation at the time of the merger. Thus, it is particularly remarkable that we still find a clear correlation between n_{GW} and SFR. This correlation is likely a consequence of the strong correlation between SFR and galaxy stellar mass (Mannucci et al. 2010).

Similarly, even if our model enforces a strong anticorrelation between the metallicity of the progenitor star and the merger rate of DBHs and BHNSs (not DNSs!), this does not imply that this anticorrelation still holds at the time of merger. Indeed, we find a correlation (instead of an anticorrelation) between n_{GW} and Z in the case of DBHs and BHNSs. As we already discussed, the latter correlation is a consequence of the mass–metallicity relation (see Figs 2 and 6).

The tight correlation between host galaxy mass and merger rate per galaxy is even more remarkable, because our model does not explicitly assume any link between the total mass of the galaxy where the compact objects merge and the merger rate.

We find that the galaxies where DBHs, BHNSs, and DNSs merge are mostly massive galaxies ($M_* \gtrsim 10^{10} M_\odot$). The galaxies where the progenitors of DNSs formed are also quite massive galaxies, while the galaxies where the progenitors of BHNSs and DBHs formed span a much larger mass range and tend to be skewed towards lower stellar masses (Fig. 8). This is in agreement with what was already found by Mapelli et al. (2018), and originates from the fact that most DBHs and BHNSs merging at $z \leq 0.1$ form from metal-poor progenitors at high redshift and merge with long time delays, while most DNSs merging at $z \leq 0.1$ form from metal-rich progenitors and merge with short time delays. Mapelli et al. (2018) combine the cosmological simulation Illustris-1 (which has lower resolution and adopts different sub-grid models with respect to the EAGLE) with the population synthesis simulation CC15 α 5 from MOBSE. Hence, the good agreement between our findings

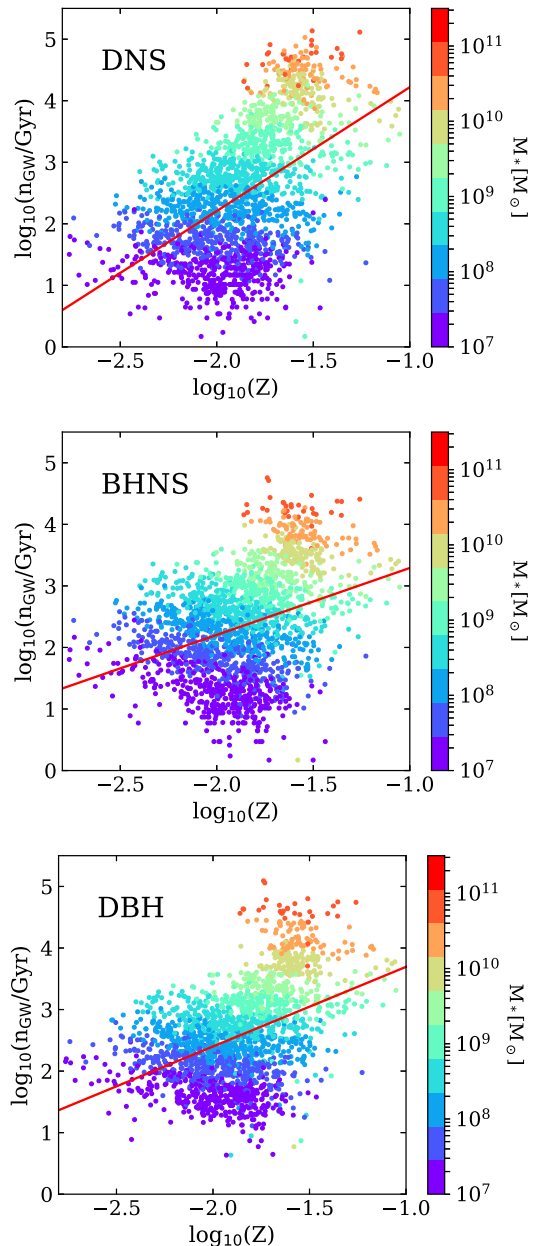


Figure 6. Merger rate per galaxy as a function of the metallicity of the host galaxy at the time the compact objects merge. The red lines represent the linear regression fits. Each point represents an individual galaxy from the EAGLE catalogue. The colour code represents the stellar mass of the galaxy.

and Mapelli et al. (2018) indicates that different resolution and different sub-grid physics in cosmological simulations do not affect our results significantly.

In Fig. 9, we plot the SFR as a function of the stellar mass of the host galaxies of DNSs, BHNSs, and DBHs. At fixed stellar mass, the host galaxies present a wide range of SFRs, while the merger rate per galaxy remains roughly the same. This reaffirms the stronger dependence of the compact object merger rate on the stellar mass with respect to the SFR.

Table 2 shows the average merger rate per galaxy as the sum over all the merger rates per galaxy divided by the total number of galaxies for different subsamples of galaxies (r_{GW}). The average

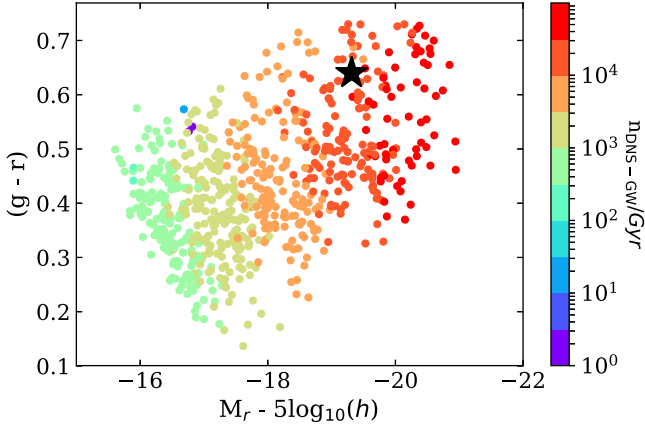


Figure 7. Colour–magnitude diagram of the host galaxies of merging DNSs at $z \leq 0.1$. Each point represents an individual galaxy from the EAGLE. The colour code represents the number of merging DNSs per Gyr in each galaxy. The black star represents the location of NGC 4993, the host galaxy of GW170817 (computed by Blanchard et al. 2017) in the colour–magnitude diagram.

merger rate r_{GW} is maximum for galaxies with both large mass ($M_* \geq 10^{10} M_\odot$) and high SFR ($\text{SFR} \geq 0.1 M_\odot \text{yr}^{-1}$), but r_{GW} is still very large even for galaxies with large mass ($M_* \geq 10^{10} M_\odot$) and low SFR ($\text{SFR} < 0.1 M_\odot \text{yr}^{-1}$) due to the strong dependence with stellar mass presented in Sections 3.2 and 3.3.

In contrast, the average specific merger rate ($r_{\text{GW}}^{\text{spec}}$, i.e. the average merger rate per unit stellar mass) shown in Table 3 is larger for small star forming galaxies, consistently with what was already found in previous work (O’Shaughnessy et al. 2017). This means that small galaxies with high star-formation rate are more efficient in producing merging binaries.

4.1 NGC 4993

The fact that the correlation between merger rate per galaxy and stellar mass is significantly steeper than the correlation between merger rate per galaxy and SFR also provides a valuable hint to understand GW170817.

It has been argued (e.g. Belczynski et al. 2018; Chruslinska et al. 2018) that finding the first DNS merger within an early-type galaxy might be in tension with models, because the SFR of NGC 4993 is low, while all models assume a correlation between the merger rate and the SFR. Our results show that the total stellar mass of the galaxy has more impact on the merger rate per galaxy than its current SFR, although our model assumed a strong correlation with the SFR at the time of progenitors’ formation.

Indeed, by looking at Figs 7 and 9, we find that the properties of NGC 4993 characterize it as one of the galaxies with the highest local merger rate per galaxy in our model. Furthermore, as discussed previously, Table 2 shows that the average merger rate r_{GW} is still large for galaxies with large mass ($M_* \geq 10^{10} M_\odot$) and low SFR ($\text{SFR} < 0.1 M_\odot \text{yr}^{-1}$), similar to NGC 4993. In particular, we predict a current DNS merger rate $\mathcal{R}_{\text{NGC4993}} \sim 3\text{--}107 \text{Myr}^{-1}$ for a galaxy with the same stellar mass and SFR as NGC 4993.

We know that ~ 36 per cent of the total stellar mass in the local Universe is locked inside elliptical galaxies (see Table 3 of Moffett et al. 2016). This percentage rises to ~ 72 per cent if we consider all early-type galaxies: not only ellipticals but also S0 and Sa galaxies

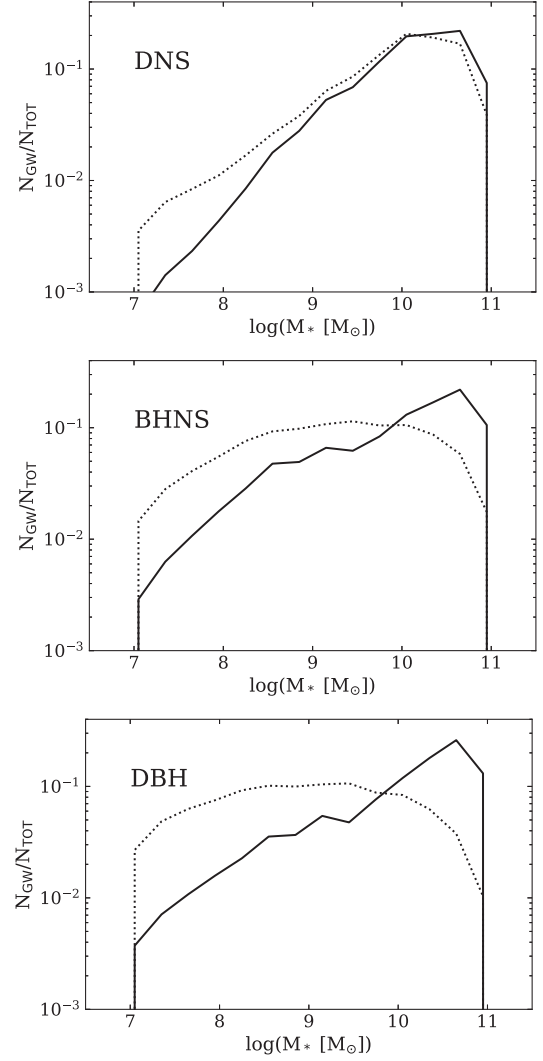


Figure 8. Stellar mass distribution of the host galaxies of merging DNSs (top), BHNSs (middle), and DBHs (bottom), where the binary systems formed (black dotted lines), and merge (black solid lines). The distribution is normalized by the total number of merging compact objects in each sample, N_{TOT} .

(NGC 4993 is an S0 galaxy; Levan et al. 2017). Thus, most stellar mass in the local Universe is located in early-type galaxies such as NGC 4993. This observational information, combined with the relatively high merger rate that we estimated for NGC 4993, helps us in understanding why the observation of the first DNS merger in an early-type galaxy is not surprising, but is in agreement with current models.

4.2 The Milky Way

From our models, a galaxy with a typical stellar mass of $\sim 5 \times 10^{10} M_\odot$ (Bland-Hawthorn & Gerhard 2016) and with a current SFR of $\sim 1.65 M_\odot \text{yr}^{-1}$, i.e. a Milky-way like galaxy (Licquia & Newman 2015), should have a typical DNS merger rate per galaxy of $\mathcal{R}_{\text{MW}} \sim 16\text{--}121 \text{Myr}^{-1}$, which is perfectly consistent with the Galactic DNS merger rate estimated by Pol et al. (2019) ($\mathcal{R}_{\text{MW}} = 42_{-14}^{+30} \text{Myr}^{-1}$).

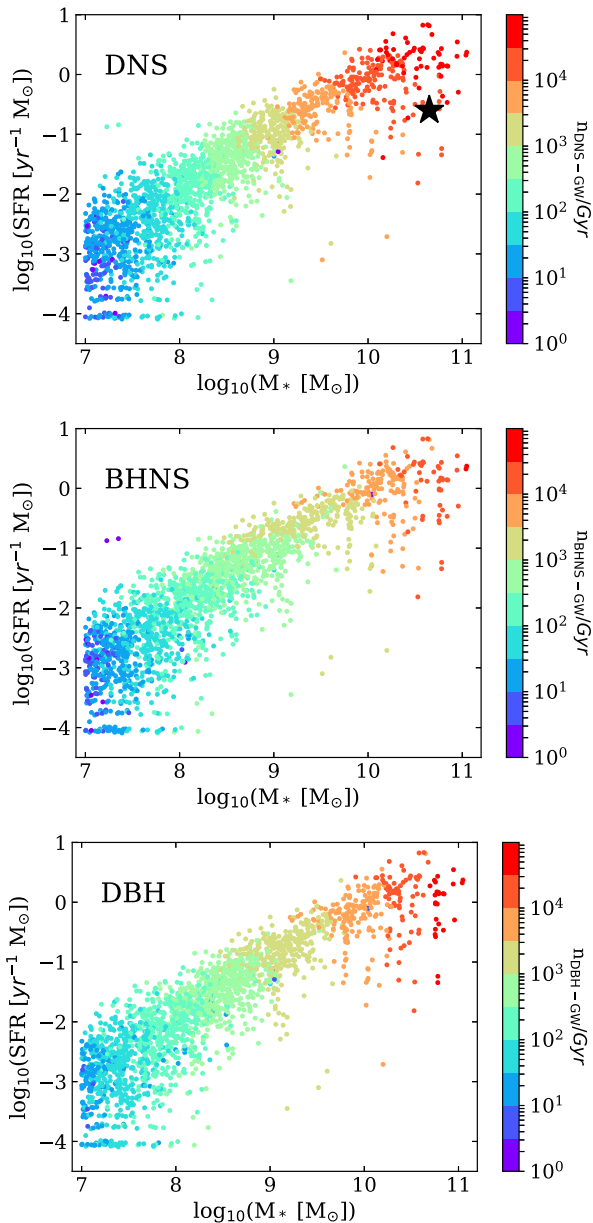


Figure 9. SFR as a function of stellar mass for the host galaxies of merging DNSs, DBHs, and BHNSs. Each point represents an individual galaxy from the EAGLE catalogue. The colour code represents the merger rate per each galaxy. The average SFR of NGC 4993 in the last Gyr (from $z \sim 0.1$ to $z = 0$) and its current stellar mass are indicated by the black star.

Thus, our main results are consistent with both the merger rate density of DNSs inferred from LIGO-Virgo and with the Galactic DNS merger rate.

4.3 The local merger rate density from the EAGLE: early-type versus late-type galaxies

Finally, we can estimate the local merger rate density directly from the EAGLE. Moreover, we can distinguish between the local merger rate density from late-type galaxies and from early-type galaxies, an information we cannot derive directly from GW detections. We stress that in the EAGLE simulation (25 Mpc box), the total stellar mass locked up in early-type galaxies and late-type galaxies is $29 \times$

$10^7 M_{\odot} \text{Mpc}^{-3} h_{0.7}$ (where $h_{0.7} = h/0.7$ is the Hubble parameter) and $8.1 \times 10^7 M_{\odot} \text{Mpc}^{-3} h_{0.7}$, respectively.³ These values are in fair agreement with observations (Moffett et al. 2016), from which we know that ~ 72 per cent of the total stellar mass in the local Universe is located in early-type galaxies.

From our results, we obtain a local DNS merger rate density $R_{\text{ET}} \sim 146 \text{Gpc}^{-3} \text{yr}^{-1} h_{0.7}$ and $R_{\text{LT}} \sim 92 \text{Gpc}^{-3} \text{yr}^{-1} h_{0.7}$ from early-type and late-type galaxies, respectively (see Table 4). Thus, the total local DNS merger rate density from the EAGLE is $\sim 238 \text{Gpc}^{-3} \text{yr}^{-1} h_{0.7}$, inside the LIGO-Virgo estimated rate ($\sim 110 - 3840 \text{Gpc}^{-3} \text{yr}^{-1}$; The LIGO Scientific Collaboration & the Virgo Collaboration 2018a).

With the same approach, we can estimate also the merger rate of DBHs and BHNSs (see Table 4). About 73 per cent (64 per cent) of all DBH (BHNS) mergers we expect in the local Universe happen in early-type galaxies, confirming the same trend as DNSs. The total local DBH merger rate density we estimate from the EAGLE is marginally too high if compared to the merger rate estimated from the LIGO-Virgo collaboration ($\sim 9.7-101 \text{Gpc}^{-3} \text{yr}^{-1}$ for DBHs and an upper limit of $\sim 610 \text{Gpc}^{-3} \text{yr}^{-1}$ for BHNSs; The LIGO Scientific Collaboration & the Virgo Collaboration 2018a), but to compare these rates more properly we should estimate the detection rate we expect from our simulations. In fact, the merger rate estimated from the LIGO-Virgo collaboration assumes a mass spectrum of BHs which is sensibly different from the mass distribution we obtain from our population-synthesis simulations (the estimated merger rate of DNSs is less affected by this problem, because the mass range of DNSs is significantly smaller than the one of DBHs).

4.4 Delay times

As a corollary of our results, we expect that the distribution of delay times t_{delay} (i.e. the time elapsed between the formation of the progenitor stars and the compact-object merger) depends on the environment of the host galaxy.

If we consider a coeval stellar population (as we obtain directly from the MOBSE simulations, before combining them with the cosmological simulation), the distribution of delay times scales approximately as $dN/dt \propto t_{\text{delay}}^{-1}$ (see e.g. Dominik et al. 2012; Giacobbo et al. 2018; Mapelli et al. 2018).

In contrast, if we consider the delay times of all compact objects merging in a given time bin (regardless of their formation redshift), the distribution of delay times can be significantly different from $dN/dt \propto t_{\text{delay}}^{-1}$. In particular, fig. 4 of Mapelli et al. (2018) shows that the distribution of delay times of compact objects merging in the local Universe can be significantly flatter than t_{delay}^{-1} , especially for DBHs and BHNSs. Similarly, Mapelli et al. (2019) suggest that >95 per cent of DBHs merging in the local Universe have $t_{\text{delay}} > 1$ Gyr (see their Table 2).

Here, we investigate the dependence of t_{delay} on the environment, and in particular on the SFR of the host galaxy. Fig. 10 shows the delay time distribution of compact objects merging in the local Universe ($z \leq 0.1$) in early-type galaxies and late-type galaxies, respectively. The two distributions are dramatically different, as expected. In particular, the delay time distribution in late-type galaxies is reminiscent of the t_{delay}^{-1} scaling, because the population of merging systems is dominated by compact objects that formed

³Here, we define early-type galaxies (late-type galaxies) as galaxies with specific SFR $\leq 10^{-10} \text{yr}^{-1}$ ($> 10^{-10} \text{yr}^{-1}$).

Table 2. Average merger rate per galaxy for the host galaxies of DNSs, BHNSs, and DBHs at the time they merge. We split the galaxy sample by stellar mass, and SFR.

	DNS	BHNS	DBH
$r_{\text{GW}}(M_* \geq 10^{10} M_{\odot} \& \text{SFR} \geq 0.1 M_{\odot} \text{ yr}^{-1})/\text{Gyr}$	34 640	9680	19 120
$r_{\text{GW}}(M_* \geq 10^{10} M_{\odot} \& \text{SFR} < 0.1 M_{\odot} \text{ yr}^{-1})/\text{Gyr}$	9920	5770	14 310
$r_{\text{GW}}(M_* < 10^{10} M_{\odot} \& \text{SFR} \geq 0.1 M_{\odot} \text{ yr}^{-1})/\text{Gyr}$	5740	1720	2430
$r_{\text{GW}}(M_* < 10^{10} M_{\odot} \& \text{SFR} < 0.1 M_{\odot} \text{ yr}^{-1})/\text{Gyr}$	210	150	240

Table 3. Average specific merger rate $r_{\text{GW}}^{\text{spec}}$ for the host galaxies of DNSs, BHNSs, and DBHs at the time they merge. We split the galaxy sample by stellar mass, SFR, and sSFR. We refer as early-type galaxies to those galaxies with $\text{sSFR} < 10^{-10} \text{ yr}^{-1}$, while late-type galaxies have an $\text{sSFR} \geq 10^{-10} \text{ yr}^{-1}$.

	DNS	BHNS	DBH
$r_{\text{GW}}^{\text{spec}}(M_* \geq 10^{10} M_{\odot} \& \text{SFR} \geq 0.1 M_{\odot} \text{ yr}^{-1})/10^7 M_{\odot} \text{ Gyr}$	5.9	1.7	3.4
$r_{\text{GW}}^{\text{spec}}(M_* \geq 10^{10} M_{\odot} \& \text{SFR} < 0.1 M_{\odot} \text{ yr}^{-1})/10^7 M_{\odot} \text{ Gyr}$	2.2	1.3	3.3
$r_{\text{GW}}^{\text{spec}}(M_* < 10^{10} M_{\odot} \& \text{SFR} \geq 0.1 M_{\odot} \text{ yr}^{-1})/10^7 M_{\odot} \text{ Gyr}$	10.1	3.1	4.4
$r_{\text{GW}}^{\text{spec}}(M_* < 10^{10} M_{\odot} \& \text{SFR} < 0.1 M_{\odot} \text{ yr}^{-1})/10^7 M_{\odot} \text{ Gyr}$	5.8	4.3	7.0
$r_{\text{GW}}^{\text{spec}}(\text{sSFR} \geq 10^{-10} \text{ yr}^{-1})/10^7 M_{\odot} \text{ Gyr}$	11.4	3.5	4.7
$r_{\text{GW}}^{\text{spec}}(\text{sSFR} < 10^{-10} \text{ yr}^{-1})/10^7 M_{\odot} \text{ Gyr}$	5.0	1.7	3.6

Table 4. Local merger rate density for early-type (R^{ET}) and late-type (R^{LT}) galaxies from the EAGLE simulation.

	R^{ET} [$\text{Gpc}^{-3} \text{ yr}^{-1}$]	R^{LT} [$\text{Gpc}^{-3} \text{ yr}^{-1}$]
DNS	146	92
BHNS	50	28
DBH	104	38

recently. In contrast, the bulk of merging compact objects in early-type galaxies has a long delay time (peaked at $t_{\text{delay}} \sim 10 \text{ Gyr}$), because the main episodes of star formation in these galaxies ended several Gyr ago. Thus, most compact objects merging in early-type galaxies in the local Universe formed several Gyr ago.

5 CONCLUSIONS

We have investigated the properties of the host galaxies of DNSs, DBHs, and BHNSs at the time they merge in the local Universe ($z \leq 0.1$), by combining the population-synthesis code MOBSE (Giacobbo et al. 2018) with galaxy catalogues from the EAGLE simulation (Schaye et al. 2015).

The results of MOBSE are consistent with compact-object masses and merger rates reported by LIGO–Virgo detections (Mapelli et al. 2017, 2018; Giacobbo & Mapelli 2018, 2019).

In this work, we focus on the stellar mass, star formation rate, metallicity, and colours of the host galaxies of compact object mergers. These are fundamental properties of the host galaxies and can help us in characterizing the environment of merging compact objects.

Our results show that the stellar mass M_* of the host galaxy is an excellent tracer of the merger rate per galaxy n_{GW} in the local Universe (Fig. 3). Massive galaxies have a higher merger rate with respect to low-mass galaxies. The star formation rate of the host galaxies also correlates with the merger rate, but the SFR– n_{GW} correlation is less tight than the M_* – n_{GW} correlation

(Fig. 4). The SFR– n_{GW} correlation is likely a mere consequence of the fact that the SFR correlates with the stellar mass of the galaxy (Fig. 9).

As a consequence, we also find a correlation of n_{GW} with the $g-r$ colour (which is a proxy of the SFR) and with the r luminosity (which is a proxy of the stellar mass) of the host galaxy (Fig. 7).

Finally, we also find a loose correlation between n_{GW} and the average metallicity Z of the host galaxy at the time of merger (Fig. 6). This correlation is a byproduct of the mass–metallicity relation of galaxies (Maiolino et al. 2008). Note that our population-synthesis models enforce an anticorrelation between progenitor’s metallicity and the merger efficiency of DBHs and BHNSs.

These correlations might be crucial for the localization of electromagnetic counterparts. Following-up on this, in a forthcoming work (Artale et al., in preparation), we will estimate the probability that a given galaxy hosts a compact-object merger as a function of its main properties.

We show that $\gtrsim 60$ per cent DNSs mergers in the local Universe are expected to happen in early-type galaxies ($R^{\text{ET}} \sim 146 \text{ Gpc}^{-3} \text{ yr}^{-1} h_{0.7}$), while only $\lesssim 40$ per cent DNSs mergers are expected in late-type galaxies ($R^{\text{LT}} \sim 92 \text{ Gpc}^{-3} \text{ yr}^{-1} h_{0.7}$). This comes from the fact that ~ 78 per cent of the stellar mass in the EAGLE box is locked up in early-type galaxies, in agreement with the observational results by Moffett et al. (2016).

In particular, NGC 4993-like galaxies (i.e. galaxies with the same stellar mass and SFR of the host galaxy of GW170817) have a merger rate per galaxy $\mathcal{R}_{\text{NGC4993}} \sim 3\text{--}107 \text{ yr}^{-1}$. Our results suggest that massive early-type galaxies like NGC 4993 are characterized by a relatively large merger rate per galaxy, due to their large mass.

Furthermore, we expect that Milky-Way like galaxies host a DNS merger rate $\mathcal{R}_{\text{MW}} \sim 16\text{--}121 \text{ Myr}^{-1}$, which is consistent with the Galactic DNS merger rate estimated by Pol et al. (2019) ($\mathcal{R}_{\text{MW}} = 42_{-14}^{+30} \text{ Myr}^{-1}$). Thus, our results are in agreement with both the DNS merger rate derived from the LIGO–Virgo collaboration (based on GW170817) and the DNS merger rate estimated from Galactic DNSs (Pol et al. 2019).

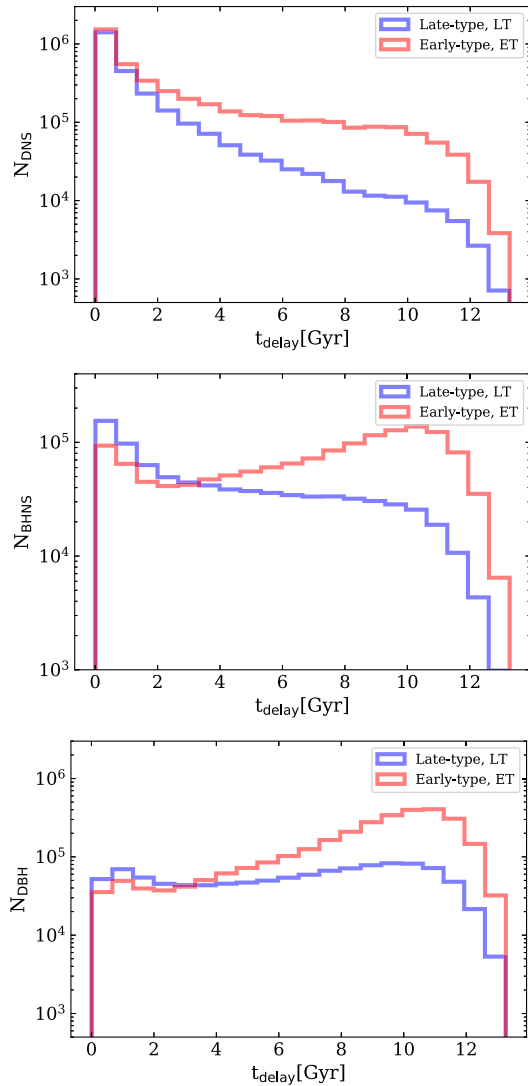


Figure 10. Distribution of delay times t_{delay} of DNSs (top), BHNSs (middle), and DBHs (bottom) in late-type (blue histogram) and early-type (red histogram) galaxies in the local Universe.

ACKNOWLEDGEMENTS

We thank the anonymous referee for their useful comments, and we are grateful to Stefania Marassi and Luca Graziani for their suggestions. MCA and MM acknowledge financial support from the Austrian National Science Foundation through FWF standalone grant P31154-N27 ‘Unraveling merging neutron stars and black hole–neutron star binaries with population synthesis simulations’. MM acknowledges financial support by the European Research Council for the ERC Consolidator grant DEMOBLACK, under contract no. 770017. MS acknowledges funding from the European Union’s Horizon 2020 research and innovation programme under the Marie-Sklodowska-Curie grant agreement No. 794393. We acknowledge the Virgo Consortium for making their simulation data available. The EAGLE simulations were performed using the DiRAC-2 facility at Durham, managed by the ICC, and the PRACE facility Curie based in France at TGCC, CEA, Bruyères-le-Châtel.

REFERENCES

- Aasi J. et al., 2015, *Class. Quantum Gravity*, 32, 074001
 Abbott B. P. et al., 2016a, *Phys. Rev. X*, 6, 041015
 Abbott B. P. et al., 2016b, *Phys. Rev. Lett.*, 116, 061102
 Abbott B. P. et al., 2016c, *Phys. Rev. Lett.*, 116, 241103
 Abbott B. P. et al., 2016d, *ApJ*, 818, L22
 Abbott B. P. et al., 2017a, *Phys. Rev. Lett.*, 118, 221101
 Abbott B. P. et al., 2017b, *Phys. Rev. Lett.*, 119, 161101
 Abbott B. P. et al., 2017c, *ApJ*, 848, L12
 Abbott B. P. et al., 2017d, *ApJ*, 848, L12
 Abbott B. P. et al., 2017e, *ApJ*, 848, L13
 Abbott B. P. et al., 2018, *Living Rev. Relativ.*, 21, 3
 Acernese F. et al., 2015, *Class. Quantum Gravity*, 32, 024001
 Alexander K. D. et al., 2017, *ApJ*, 848, 69
 Antonini F., Rasio F. A., 2016, *ApJ*, 831, 187
 Antonini F., Gieles M., Gualandris A., 2019, *MNRAS*, 486, 5008
 Askar A., Szkudlarek M., Gondek-Rosińska D., Giersz M., Bulik T., 2017, *MNRAS*, 464, L36
 Askar A., Arca Sedda M., Giersz M., 2018, *MNRAS*, 478, 1844
 Banerjee S., 2017, *MNRAS*, 467, 524
 Banerjee S., 2018, *MNRAS*, 473, 909
 Banerjee S., Baumgardt H., Kroupa P., 2010, *MNRAS*, 402, 371
 Bartos I., Kocsis B., Haiman Z., Márka S., 2017, *ApJ*, 835, 165
 Belczynski K. et al., 2018, preprint ([arXiv:1812.10065](https://arxiv.org/abs/1812.10065))
 Belczynski K., Kalogera V., Bulik T., 2002, *ApJ*, 572, 407
 Belczynski K., Perna R., Bulik T., Kalogera V., Ivanova N., Lamb D. Q., 2006, *ApJ*, 648, 1110
 Belczynski K., Taam R. E., Kalogera V., Rasio F. A., Bulik T., 2007, *ApJ*, 662, 504
 Belczynski K., Kalogera V., Rasio F. A., Taam R. E., Zezas A., Bulik T., Maccarone T. J., Ivanova N., 2008, *ApJS*, 174, 223
 Belczynski K., Bulik T., Fryer C. L., Ruiter A., Valsecchi F., Vink J. S., Hurley J. R., 2010, *ApJ*, 714, 1217
 Belczynski K., Holz D. E., Bulik T., O’Shaughnessy R., 2016, *Nature*, 534, 512
 Beniamini P., Piran T., 2016, *MNRAS*, 456, 4089
 Beniamini P., Hotokezaka K., Piran T., 2016, *ApJ*, 832, 149
 Bethe H. A., Brown G. E., 1998, *ApJ*, 506, 780
 Blanchard P. K. et al., 2017, *ApJ*, 848, L22
 Bland-Hawthorn J., Gerhard O., 2016, *ARA&A*, 54, 529
 Bogomazov A. I., Lipunov V. M., Tutukov A. V., 2007, *Astron. Rep.*, 51, 308
 Camps P. et al., 2018, *ApJS*, 234, 20
 Camps P., Trayford J. W., Baes M., Theuns T., Schaller M., Schaye J., 2016, *MNRAS*, 462, 1057
 Cao L., Lu Y., Zhao Y., 2018, *MNRAS*, 474, 4997
 Chen Y., Bressan A., Girardi L., Marigo P., Kong X., Lanza A., 2015, *MNRAS*, 452, 1068
 Chornock R. et al., 2017, *ApJ*, 848, L19
 Chruslinska M., Belczynski K., Klencki J., Benacquista M., 2018, *MNRAS*, 474, 2937
 Colpi M., Mapelli M., Possenti A., 2003, *ApJ*, 599, 1260
 Coulter D. A. et al., 2017, *Science*, 358, 1556
 Cowperthwaite P. S. et al., 2017, *ApJ*, 848, L17
 Crain R. A. et al., 2015, *MNRAS*, 450, 1937
 de Mink S. E., Belczynski K., 2015, *ApJ*, 814, 58
 de Mink S. E., Mandel I., 2016, *MNRAS*, 460, 3545
 De Rossi M. E., Bower R. G., Font A. S., Schaye J., Theuns T., 2017, *MNRAS*, 472, 3354
 Del Pozzo W., Berry C. P. L., Ghosh A., Haines T. S. F., Singer L. P., Vecchio A., 2018, *MNRAS*, 479, 601
 Di Carlo U. N., Giacobbo N., Mapelli M., Pasquato M., Spera M., Wang L., Haardt F., 2019, preprint ([arXiv:1901.00863](https://arxiv.org/abs/1901.00863))
 Dominik M. et al., 2015, *ApJ*, 806, 263
 Dominik M., Belczynski K., Fryer C., Holz D. E., Berti E., Bulik T., Mandel I., O’Shaughnessy R., 2012, *ApJ*, 759, 52

- Dominik M., Belczynski K., Fryer C., Holz D. E., Berti E., Bulik T., Mandel I., O’Shaughnessy R., 2013, *ApJ*, 779, 72
- Downing J. M. B., Benacquista M. J., Giersz M., Spurzem R., 2010, *MNRAS*, 407, 1946
- Downing J. M. B., Benacquista M. J., Giersz M., Spurzem R., 2011, *MNRAS*, 416, 133
- Dvorkin I., Vangioni E., Silk J., Uzan J.-P., Olive K. A., 2016, *MNRAS*, 461, 3877
- Elbert O. D., Bullock J. S., Kaplinghat M., 2018, *MNRAS*, 473, 1186
- Eldridge J. J., Stanway E. R., 2016, *MNRAS*, 462, 3302
- Eldridge J. J., Stanway E. R., Tang P. N., 2019, *MNRAS*, 482, 870
- Farr W. M., Sravan N., Cantrell A., Kreidberg L., Bailyn C. D., Mandel I., Kalogera V., 2011, *ApJ*, 741, 103
- Flannery B. P., van den Heuvel E. P. J., 1975, *A&A*, 39, 61
- Fryer C. L., Belczynski K., Wiktorowicz G., Dominik M., Kalogera V., Holz D. E., 2012, *ApJ*, 749, 91
- Giacobbo N., Mapelli M., 2018, *MNRAS*, 480, 2011
- Giacobbo N., Mapelli M., 2019, *MNRAS*, 482, 2234
- Giacobbo N., Mapelli M., Spera M., 2018, *MNRAS*, 474, 2959
- Goldstein A. et al., 2017, *ApJ*, 848, L14
- Gräferer G., Vink J. S., de Koter A., Langer N., 2011, *A&A*, 535, A56
- Guo Q. et al., 2011, *MNRAS*, 413, 101
- Hurley J. R., Pols O. R., Tout C. A., 2000, *MNRAS*, 315, 543
- Hurley J. R., Tout C. A., Pols O. R., 2002, *MNRAS*, 329, 897
- Hurley J. R., Sippel A. C., Tout C. A., Aarseth S. J., 2016, *Publ. Astron. Soc. Aust.*, 33, e036
- Im M. et al., 2017, *ApJ*, 849, L16
- Kelley L. Z., Blecha L., Hernquist L., 2017, *MNRAS*, 464, 3131
- Kimpson T. O., Spera M., Mapelli M., Ziosi B. M., 2016, *MNRAS*, 463, 2443
- Knigge C., Coe M. J., Podsiadlowski P., 2011, *Nature*, 479, 372
- Kruckow M. U., Tauris T. M., Langer N., Kramer M., Izzard R. G., 2018, *MNRAS*, 481, 1908
- Kulkarni S. R., Hut P., McMillan S., 1993, *Nature*, 364, 421
- Kumamoto J., Fujii M. S., Tanikawa A., 2019, *MNRAS*, 486, 3942
- Lamberts A. et al., 2018, *MNRAS*, 480, 2704
- Lamberts A., Garrison-Kimmel S., Clausen D. R., Hopkins P. F., 2016, *MNRAS*, 463, L31
- Levan A. J. et al., 2017, *ApJ*, 848, L28
- Licquia T. C., Newman J. A., 2015, *ApJ*, 806, 96
- Maiolino R. et al., 2008, *A&A*, 488, 463
- Mannucci F., Cresci G., Maiolino R., Marconi A., Gnerucci A., 2010, *MNRAS*, 408, 2115
- Mapelli M., 2016, *MNRAS*, 459, 3432
- Mapelli M., Giacobbo N., 2018, *MNRAS*, 479, 4391
- Mapelli M., Zampieri L., 2014, *ApJ*, 794, 7
- Mapelli M., Colpi M., Zampieri L., 2009, *MNRAS*, 395, L71
- Mapelli M., Ripamonti E., Zampieri L., Colpi M., Bressan A., 2010, *MNRAS*, 408, 234
- Mapelli M., Zampieri L., Ripamonti E., Bressan A., 2013, *MNRAS*, 429, 2298
- Mapelli M., Giacobbo N., Ripamonti E., Spera M., 2017, *MNRAS*, 472, 2422
- Mapelli M., Giacobbo N., Toffano M., Ripamonti E., Bressan A., Spera M., Branchesi M., 2018, *MNRAS*, 481, 5324
- Mapelli M., Giacobbo N., Santoliquido F., Artale M. C., 2019, *MNRAS*, 487, 1108
- Marassi S., Graziani L., Ginolfi M., Schneider R., Mapelli M., Spera M., Alparone M., 2019, *MNRAS*, 484, 3219
- Marchant P., Langer N., Podsiadlowski P., Tauris T. M., Moriya T. J., 2016, *A&A*, 588, A50
- Margutti R. et al., 2017, *ApJ*, 848, L20
- McAlpine S. et al., 2016, *Astron. Comput.*, 15, 72
- McKernan B., Ford K. E. S., Lyra W., Perets H. B., 2012, *MNRAS*, 425, 460
- Mennekens N., Vanbeveren D., 2014, *A&A*, 564, A134
- Moffett A. J. et al., 2016, *MNRAS*, 462, 4336
- Moody K., Sigurdsson S., 2009, *ApJ*, 690, 1370
- Nicholl M. et al., 2017, *ApJ*, 848, L18
- Oliphant T. E., 2006, *A guide to NumPy*. Vol. 1. Trelgol Publishing, USA
- O’Leary R. M., Rasio F. A., Fregeau J. M., Ivanova N., O’Shaughnessy R., 2006, *ApJ*, 637, 937
- O’Leary R. M., Kocsis B., Loeb A., 2009, *MNRAS*, 395, 2127
- O’Leary R. M., Meiron Y., Kocsis B., 2016, *ApJ*, 824, L12
- O’Shaughnessy R., Kalogera V., Belczynski K., 2010, *ApJ*, 716, 615
- O’Shaughnessy R., Bellovary J. M., Brooks A., Shen S., Governato F., Christensen C. R., 2017, *MNRAS*, 464, 2831
- Özel F., Psaltis D., Narayan R., McClintock J. E., 2010, *ApJ*, 725, 1918
- Perna R., Belczynski K., 2002, *ApJ*, 570, 252
- Perna R., Chruslinska M., Corsi A., Belczynski K., 2018, *MNRAS*, 477, 4228
- Pfahl E., Rappaport S., Podsiadlowski P., Spruit H., 2002, *ApJ*, 574, 364
- Pian E. et al., 2017, *Nature*, 551, 67
- Planck Collaboration XVI, 2014, *A&A*, 571, A16
- Podsiadlowski P., Langer N., Poelarends A. J. T., Rappaport S., Heger A., Pfahl E., 2004, *ApJ*, 612, 1044
- Podsiadlowski P., Dewi J. D. M., Lesaffre P., Miller J. C., Newton W. G., Stone J. R., 2005, *MNRAS*, 361, 1243
- Pol N., McLaughlin M., Lorimer D. R., 2019, *ApJ*, 870, 71
- Portegies Zwart S. F., McMillan S. L. W., 2000, *ApJ*, 528, L17
- Portegies Zwart S. F., Yungelson L. R., 1998, *A&A*, 332, 173
- Rasskazov A., Kocsis B., 2019, preprint ([arXiv:1902.03242](https://arxiv.org/abs/1902.03242))
- Rastello S., Amaro-Seoane P., Arca-Sedda M., Capuzzo-Dolcetta R., , , Fragione G., Melo I. T. e., 2019, *MNRAS*, 483, 1233
- Rodriguez C. L., Morscher M., Pattabiraman B., Chatterjee S., Haster C.-J., Rasio F. A., 2015, *Phys. Rev. Lett.*, 115, 051101
- Rodriguez C. L., Chatterjee S., Rasio F. A., 2016, *Phys. Rev. D*, 93, 084029
- Rodriguez C. L., Amaro-Seoane P., Chatterjee S., Kremer K., Rasio F. A., Samsing J., Ye C. S., Zevin M., 2018, *Phys. Rev. D*, 98, 123005
- Sadowski A., Belczynski K., Bulik T., Ivanova N., Rasio F. A., O’Shaughnessy R., 2008, *ApJ*, 676, 1162
- Safarzadeh M., Berger E., 2019, preprint ([arXiv:1904.08436](https://arxiv.org/abs/1904.08436))
- Samsing J., 2018, *Phys. Rev. D*, 97, 103014
- Savchenko V. et al., 2017, *ApJ*, 848, L15
- Schaye J. et al., 2015, *MNRAS*, 446, 521
- Schneider R., Graziani L., Marassi S., Spera M., Mapelli M., Alparone M., Bennassuti M. de., 2017, *MNRAS*, 471, L105
- Shao Y., Li X.-D., 2018, *MNRAS*, 477, L128
- Sigurdsson S., Hernquist L., 1993, *Nature*, 364, 423
- Sigurdsson S., Phinney E. S., 1995, *ApJS*, 99, 609
- Soares-Santos M. et al., 2017, *ApJ*, 848, L16
- Spera M., Mapelli M., 2017, *MNRAS*, 470, 4739
- Spera M., Mapelli M., Bressan A., 2015, *MNRAS*, 451, 4086
- Spera M., Mapelli M., Giacobbo N., Trani A. A., Bressan A., Costa G., 2019, *MNRAS*, 485, 889
- Stevenson S., Vigna-Gómez A., Mandel I., Barrett J. W., Neijssel C. J., Perkins D., de Mink S. E., 2017, *Nat. Commun.*, 8, 14906
- Stone N. C., Metzger B. D., Haiman Z., 2017, *MNRAS*, 464, 946
- Tauris T. M. et al., 2017, *ApJ*, 846, 170
- Tauris T. M., Langer N., Podsiadlowski P., 2015, *MNRAS*, 451, 2123
- The LIGO Scientific Collaboration, the Virgo Collaboration, 2018a, preprint ([arXiv:1811.12907](https://arxiv.org/abs/1811.12907))
- The LIGO Scientific Collaboration, The Virgo Collaboration, 2018b, preprint ([arXiv:1811.12940](https://arxiv.org/abs/1811.12940))
- Tutukov A., Yungelson L., 1973, *Nauchnye Inf.*, 27, 70
- van den Heuvel E. P. J., 2007, in di Salvo T., Israel G. L., Piersant L., Burderi L., Matt G., Tornambe A., Menna M. T., eds, *AIP Conf. Ser. Vol. 924, The Multicolored Landscape of Compact Objects and Their Explosive Origins*, Am. Inst. Phys., New York, p. 598
- van der Walt S., Colbert S. C., Varoquaux G., 2011, *Comput. Sci. Eng.*, 13, 22

Vink J. S., 2017, *Philos. Trans. R. Soc. Lond. A*, 375, 0160269

Vink J. S., de Koter A., 2005, *A&A*, 442, 587

Vink J. S., de Koter A., Lamers H. J. G. L. M., 2001, *A&A*, 369, 574

Vogelsberger M. et al., 2014, *MNRAS*, 444, 1518

Voss R., Tauris T. M., 2003, *MNRAS*, 342, 1169

Woosley S. E., 2017, *ApJ*, 836, 244

Zevin M., Pankow C., Rodriguez C. L., Sampson L., Chase E., Kalogera V., Rasio F. A., 2017, *ApJ*, 846, 82

Ziosi B. M., Mapelli M., Branchesi M., Tormen G., 2014, *MNRAS*, 441, 3703

This paper has been typeset from a $\text{\TeX}/\text{\LaTeX}$ file prepared by the author.